JOM, Vol. 65, No. 12, 2013
DOI: 10.1007/s11837-013-0777-y

Solar Carboreduction of Alumina Under Vacuum

IRINA VISHNEVETSKY,[1,3] RAMI BEN-ZVI,[2] MICHAEL EPSTEIN,[2] SHMUEL BARAK,[2] and RACHAMIM RUBIN[2]

1.—Department of Earth and Planetary Sciences, Weizmann Institute of Science, POB 26, 76100 Rehovot, Israel. 2.—Solar Research Facilities Unit, Weizmann Institute of Science, POB 26, 76100 Rehovot, Israel. 3.—e-mail: irina.vishnevetsky@weizmann.ac.il

A preliminary study on carboreduction of alumina under vacuum, which was necessary before the solar reactor design, has been performed using an induction heater equipped with a graphite susceptor as the sample holder surrounded by a ceramic tube serving as the metal vapor deposit site. The primary objective was to study the forward and backward reactions as a function of temperature and CO partial pressure. It was concluded that at reaction temperatures above 1600°C and at an average CO partial pressure below 0.2 mbar, the amount of residual by-products in the graphite crucible was negligible, whereas tests with an average CO partial pressure of 2.6 mbar required temperatures above 1800°C to convert the stoichiometric reactants pellets fully. It was concluded that pure aluminum can be found only at deposit sites with temperatures below 600–700°C in tests with temperature and pressure suitable to prevent the volatile suboxide formation in the forward reaction. Based on these results, the solar reactor was designed with a sharp temperature drop from the hot to the cold area. The results of solar tests with different levels of CO partial pressure and temperature conditions reveal that the alumina to aluminum conversion is about 90% for reaction temperatures above the minimum temperature required for full conversion as predicted by the thermodynamic calculations at the appropriate pressure. However, at lower temperatures, a significant amount of solid Al_4C_3, Al_4CO_4, and volatile Al_2O can be formed in the forward reaction, leading to an increase of the residual by-product in the reactant holder as well as lower purity of the aluminum product and an increase of the alumina content in the deposits at the cold reactor's zone. The observed nanocrystalline and amorphous morphology of the deposits caused by fast cooling in the cold zone will also be discussed.

INTRODUCTION

Aluminum (Al) is an element with strong metal-oxygen bonds. The reduction of aluminum oxide to Al can produce undesirable by-products (volatile aluminum suboxide, carbide, and oxycarbide) and demands high energy input. Therefore, solar thermal carboreduction can be considered as a promising option when at least part of the necessary energy can be provided from concentrated solar radiation. The high reaction temperature that this process requires at atmospheric pressure poses a major difficulty. According to Le Chatelier's principle, decreasing the partial pressure of the product gases to vacuum conditions reduces the reaction temperature, but this requires additional energy input for the pumping. It was estimated[1] that for CO partial pressure below 0.2 mbar, the pumping energy significantly exceeds the energy consumption in the commercial electrolytic process and the theoretical work of exothermal expansion. Pumping energy approaches the theoretical work only when the CO partial pressure exceeds 1 mbar. At this pressure, the total energy demand (solar energy required for the preheating and chemical reaction, and electrical energy for vacuum pumping) approaches the energy consumption in the electrolytic process.

The thermodynamics of the thermocarboreduction of alumina under vacuum conditions has been discussed[2–4] and preliminary experimental results have been reported previously.[1,3–6] Complementary investigations over a wide range of temperatures

(Published online October 8, 2013)

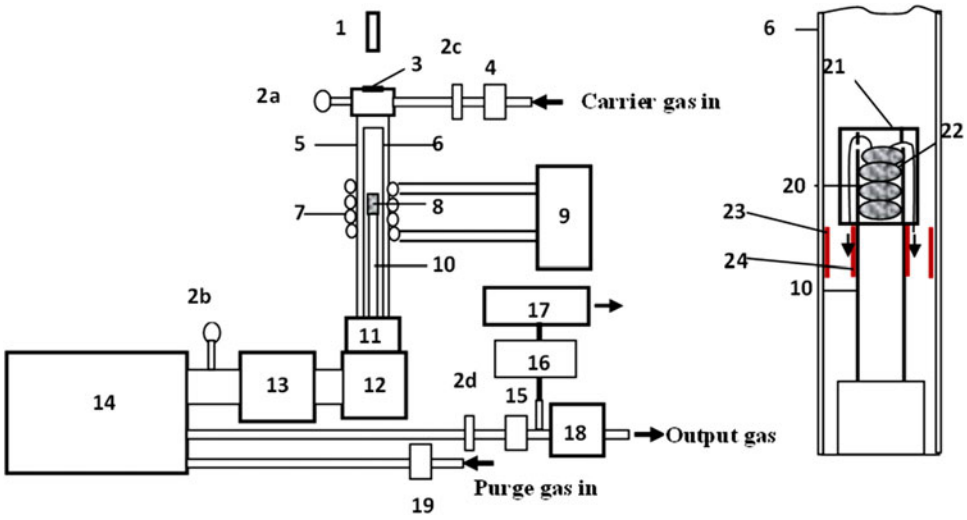

Fig. 1. A scheme of the experimental setup (a): 1-pyrometer, 2a, b-vacuum gauges, 2c, d-pressure transmitters, 3-quartz window, 4, 19-flow in controllers, 5-quartz tube, 6-ceramic tube, 7-induction coil, 8-graphite susceptor, 9-induction heater, 10-pedestal molybdenum tube with alumina insulation support, 11-water cooled trap, 12-filter, 13-liquid nitrogen trap, 14-dry vacuum system, 15-flow out meter, 16-diaphragm pump, 17-gas chromatograph, 18-IR analyzer; graphite susceptor: 20-inner graphite crucible, 21-outer graphite crucible cap, 22-reaction pellets, 23, 24-deposit sites.

and pressures in a laboratory and under solar conditions are required before conclusions can be drawn about the potential commercial implementation of solar alumina carboreduction under vacuum.

THERMODYNAMICS

The main challenges associated with alumina carboreduction that have been predicted thermodynamically[7] and presented in details previously[1,6] can be summarized as follows:

- Despite vacuum below 1 mbar, a high reaction temperature up to 1800°C (and high energy input) is required to achieve full conversion of alumina.
- The high condensation temperature of aluminum vapor can promote reoxidation and carbonization in reverse reactions of the product metal.
- The relatively high volume of product gas released per unit weight of produced Al requires significant pumping power.
- Complex chemistry during the forward and/or backward reactions leads to the formation of by-products such as aluminum oxycarbide, carbide, and volatile suboxide.

If the temperature of the forward reaction is lower than the temperature required for full conversion, then the formation of volatile aluminum suboxide in the forward reaction conjugates with its transformation to alumina and aluminum during deposition at cold sites at a relatively low temperature according to:

$$3Al_2O(g) = Al_2O_3 + 4Al \quad (1)$$

Interaction of liquid aluminum deposited on hotter sites with product CO can form aluminum oxide, carbide, and oxycarbide.

PRELIMINARY INVESTIGATION USING INDUCTION HEATING FURNACE

Experimental Setup

Experimental setup with a 25-kW desktop induction heater (IH) with dry vacuum system (DVS) have been described in detail previously[6] and are presented schematically in Fig. 1.

The composition in the outlet gases was recorded every 10 s. Tests were stopped when the CO content approached zero, and the amount of residual products in the forward reaction was estimated by weighing the crucible before and after the tests. The aluminum content and by-products formation in the reverse reactions were determined by X-ray diffraction (XRD) quantitative analysis of the deposits obtained at various sites having different temperatures.

Stoichiometric reactants mixtures were prepared using wood charcoal as biomass source, 10 μm alumina powder (by Sigma-Aldrich, St. Louis, MO, USA), and 10 wt.% sugar powder as a binder. The mixture was pressed under 10 tons to form pellets. After pressing, the pellets were baked at 165°C for 20 min.

In the tests performed, the temperatures were varied from 1400°C to 1800°C and maximal CO partial pressure varied from 4 mbar to 0.05 mbar. Pressure was regulated by opening the vacuum valve at the entrance of the DVS to various degrees. The mass of the pellets loaded inside the graphite crucible was approximately 3–3.5 g in each test, and the flow rate of the argon carrier gas was varied from 0.1 L/min to 1 L/min.

Experimental Results

Output gases consist of the CO, hydrogen, and small amount of methane. The CO appeared in two

peaks. The first peak of CO appeared together with H_2 and CH_4 during the preheating and originated from the sugar and impurities in the charcoal. The second, and larger, peak of CO contains oxygen atoms from the alumina. The reaction time was defined as the interval of time from the beginning to the end of the second CO peak, and it was used to average the reaction temperature and CO partial pressure as a function of time (Eq. 3). The useful oxygen yield was estimated as the ratio of O-atoms in the CO originating from alumina (the second CO peak) to the amount of O-atoms in the reacted alumina (Eq. 4). This parameter is usually higher than the real aluminum yield (Eq. 5) because of the formation of carbide and oxycarbide. It should be noted that in case of carboreduction of metal oxides with simpler chemistry, e.g., ZnO and MgO, the results of both the oxygen and the metal yield estimations coincide within the measurements inaccuracy.

The main test parameters have been listed and discussed in detail previously.[1]

Increasing the argon carrier gas flow rate is undesirable when the resistance upstream the DVS is relatively small because it increases the required pumping power. However, increasing the argon flow rate tenfold at the same test temperature increases the yield of pure Al by about 10% (because of the decrease in the CO partial pressure) and extends the size of deposit sites 23 and 24 (Fig. 1) by about 30% toward colder areas.

The reaction kinetics was estimated by comparing the interval of time spanned by the second CO peak at half of its height. Time values rapidly decrease from 80 min to 5 min with increasing the reaction temperature from 1400°C to 1850°C. Although the time duration at half of the peak height does not depend on the CO partial pressure, the total reaction time increases for a higher CO partial pressure at the same temperature.

Forward Reaction

The extent of the forward reaction was estimated by examining the residue remained in the reactant crucible, 20 (Fig. 1), over the range of temperatures and pressures. The mass of the residue was negligible when the minimum temperature in the reaction zone is above 1500°C with CO average/maximum partial pressure was below 0.2/0.5 mbar, respectively. For CO partial pressure higher than 0.8/1.7 mbar, the minimum temperature in the reaction zone should be higher than 1700°C to minimize residue.

Backward Reaction

The aluminum vapor leaving the crucible condenses near and below the susceptor at hot deposit sites 23 and 24 (Fig. 1) because the condensation temperature of aluminum vapor is high even under vacuum conditions. The high temperature at these locations stimulates the back reaction of the condensed aluminum. The amount of pure aluminum remaining at the end of the test depends on the temperature at the deposit site, and it predominates in the outer layers of the deposit. According to the visual examination, scanning electron microscopy (SEM) images, and XRD analysis, pure aluminum is observed as drops larger than 100 μm while Al with 70–90% purity appears as smaller drops and conglomerates of gray powder. The samples scraped off the hottest sites, where the temperature is conducive to not only condensation of aluminum vapor but also strong reverse reactions, appear as yellowish powders. The Al content of these powders is lower than that of the gray deposits, reaching zero in the yellow-orange powder that contains only aluminum carbide and oxycarbide.

Theoretical Estimation of the Temperature Distribution in IH Reactor

To determine the relationship between the temperatures at different locations inside the IH reactor with the extent of the reverse reactions and to correlate the temperatures measured by means of noncontact sensor to the actual reaction temperature, a heat transfer modeling using the Elmer finite-element package was developed and applied.[1] It was substituted by ANSYS Fluent volume element package (ANSYS, Inc., Canonsburg, PA, USA)[8] due to its more appropriate modeling capabilities. Fluent allows treating heat transfer by applying several methods, the most general of which is the discrete ordinates (DO). This method is used here because it allows modeling semitransparent media with spectral effects and boundaries having both diffuse and specular reflections, thus enabling appropriate treatment of the quartz parts (the quartz tube and the window).

The void zones between the solid parts are modeled as an artificial fully transparent, nonscattering, and nonrefracting (refractive index, $n = 1$) medium with low conductivity (0.00242 W/m–K, i.e., 1/10 of the air conductivity), named "vacuum." This is required because the DO intensity can only pass through a medium.

Quartz has an almost abrupt transmissivity change in the near infrared (NIR). Based on data from various manufacturer's catalogues [GE Fused Quartz for GE-124 (GE, Willoughby, OH, USA), WQS Clear Fused Tubing Type 214 (GE), and Heraeus Quarzglas Suprasil (Heraeus Quarzglas, Hanau. Germany)], a two-band model was calibrated with cutoff wavelength of 3.697 μm, refraction index n of 1.454 and 1.265, and absorption coefficient κ of 4.8 m^{-1} and 925.6 m^{-1} for the low and high bands, respectively. It is assumed to be nonscattering. At its boundaries, fully specular Fresnel-type boundary conditions are used.

The 4-mm-thick ceramic pipe was found to be partially transparent with transmission estimated at 30%, so extinction coefficient of 300 m^{-1} was

Table I. Calculation of the temperature and emissivity (FLUENT Model) for three source levels

No.	Crucible material	Ceramic pipe material	Source, S_v (W/m^3) × 10^{-8}	T_{real} at measurement location (°C)	$T_{reaction\ zone}$ (°C)	ε_{app}	T_{meas} (°C)
1	Graphite	Zirconia	1	1294	1322	0.8857	1218
2	Graphite	Zirconia	2	1564	1657	0.8866	1462
3	Graphite	Zirconia	3	1738	1886	0.8873	1618

taken. In the absence of better data, half of this value is deemed due to absorption and the rest due to scattering, assumed isotropic here. A refraction index of $n = 1$ is assumed for the ceramic pipe and gray optical properties.

The pyrometer is modeled as a copper disk with its top (external) face held at $T = 1$ K and its side insulated. The region between the pyrometer and the window is modeled as a "vacuum" cylinder with a black-body radiating side to $T = 1$ K ambient surroundings. The pyrometer is sensitive to incident radiation at 2.2 μm, so a spectral band 2.1–2.3 μm was added to the DO model.

The external surfaces of the device (quartz tube) are radiating to the 300 K surrounding at the appropriate surface emissivities, except the water-cooled channel in the bottom flange side—which is held at $T = 300$ K.

The grid used by Fluent had 28253 nodes and 24829 cells. The directional grid had 4 × 4 ordinates (each divided into 4 × 4 pixels) in each directional space octant. It was verified that the solution is grid independent for this grid.

The results were postprocessed by a special-purpose code developed to calculate by view factors the incident and outgoing fluxes from desired element faces, given their optical properties. In this way, the apparent emissivity of the region viewed by the pyrometer is predicted. Using the Plank low equation, it is possible to get that the real temperature of this region T_{real} is related to the pyrometer measured temperature T_{meas} via

$$T_{meas} = \frac{c_2}{\lambda \ln\left[(e^{C_2/\lambda T_{real}} - 1)/(k\varepsilon) + 1\right]} \qquad (2)$$

In Eq. 2, $\lambda = 2.2$ μm is the pyrometer sensor wavelength, ε is the apparent emissivity, $k = 0.91$ is the attenuation factor due to absorption and reflection in the quartz window, and $c_2 = 0.01439$ m∗K is a second radiation constant.

It was assumed that the crucible is completely filled with reactants pellets to estimate the temperature distribution in the reaction zone. Temperature distribution along all parts of the IH was calculated for the three various values of uniform volumetric source levels, Sv (see in Table I). Temperature distributions along the ceramic pipe internal surface, the pedestal molybdenum pipe external surface, and the pellets are shown in Fig. 2

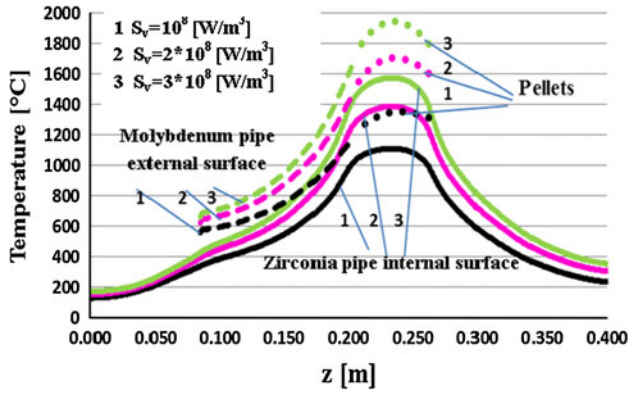

Fig. 2. Temperature distribution in the IH reactor along the internal surface of zirconia tube, external surface of Mo tube and reactant pellets for three S_v values.

for the three source levels that were applied at the vertical part of the external crucible cap. Correlations of real temperatures to the measured temperature allow interpolation of actual experiments to available calculation results. This enables estimating real temperature at deposit sites.

The apparent emissivity as seen from the pyrometer is calculated from view factors and temperatures as calculated by the ELMER finite elements package (CSC, Espoo, Finland)[9] used in a preliminary study.[1] Radiation exchange within the cavity is done by application of view factors[10] and is modified for semitransparent surfaces.

Amount of Pure Aluminum as a Function of Temperature at Different Deposit Sites

Figure 3 presents the weight percent of pure aluminum in samples at a deposit site as a function of the temperature on the internal surface of the zirconia tube and on the external surface of the molybdenum tube. The temperature at each deposit site was interpolated from calculated results for tests with average CO partial pressure less than 0.2 mbar. It can be concluded that to avoid oxidation and carbonization of the condensed aluminum, temperatures below 600–700°C are desirable at the deposit sites when CO partial pressure is around few tenths of a millibar. Figure 3 also shows that at sites with similar temperatures, a higher percentage of pure aluminum can be obtained when there is higher CO partial pressure, which corresponds to a higher reaction temperature and shorter reaction time.

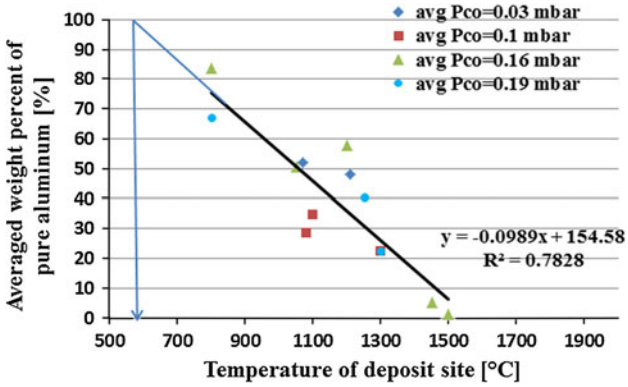

Fig. 3. Amount of pure aluminum as function of temperature at deposit sites containing Al, Al_4C_3, and Al_4CO_4 for tests with averaged CO partial pressure lower than 0.2 mbar.

The analysis of the IH reactor reveals system properties that can be applied to the solar system to optimize the yield of pure Al; consequently, the solar reactor should provide a high enough temperature in the reaction zone to achieve fast kinetics, relatively high temperature in the transition zone to prevent aluminum vapor deposition where backward reactions can take place, and a sharp drop in temperature toward the deposit sites where the backward reactions can be minimized.

THE SOLAR REACTOR

The Main Features of the Solar Reactor

It was concluded from the experimental results described above that the characteristics of the solar reactor should include the following:

1. A high temperature (up to 1800°C) in the reaction zone must be achieved with the aid of solar concentrating optics that can reach the level of 5000 suns.
2. A relatively low temperature (less than 600–700°C) at the main product deposit site.
3. A transition region of minimal size between the hot reaction area and the cold deposit site to suppress backward reaction efficiently.
4. Reactor parts, especially the quartz window, resistant to thermal stresses and pressure caused by the internal vacuum and the perpendicular traction forces (2 bars) applied by the side seal.

Concentrating Optics

The concentrating facility (>5000 suns) available at the Weizmann Solar Tower was exploited. Its principal optical scheme is presented in Fig. 4: a heliostat reflects solar energy on the concentrating parabolic dish through an intermediate flat mirror. Concentrated solar light enters the reactor through a spherically shaped quartz window that can withstand the internal vacuum conditions, and then it passes through a zirconia aperture placed at the focal plane of the dish (Fig. 5a).

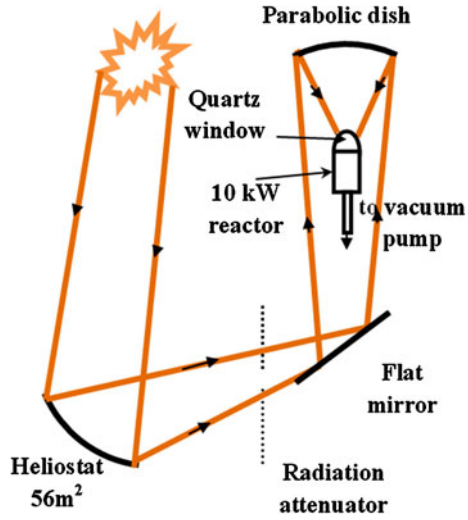

Fig. 4. Schematic layout of the concentrating optics.

Solar Reactor Design

The solar reactor was designed based on the Fluent model mentioned above[8] to meet the previously discussed specifications (see the "The Main Features of the Solar Reactor" section).

A general cross section of the solar reactor is presented in Fig. 5a. The reactor contains a graphite cover to prevent product vapors released from the reactant holder from settling on the quartz window, a graphite cone that serves as part of the hot zone, and a water-cooled stainless steel tube (0.05 m diameter) that functions as the main cold deposit site for aluminum vapors. Further details are presented in Fig. 5b, which illustrates the sealing arrangement of the quartz window, the radiation shield to protect the sealing area, the graphite cover and crucible (pellets holder), the graphite tube and cone leading to the exit, the zirconia insulation and aperture, the reaction pellets, the location of a thermocouple (one of the eight shown in Fig. 5b), and cooling water for the flange with the window seals. Figure 5b also shows the path of the carrier gas up along the inner window surface, then down to passage holes in the graphite cover and into the graphite cone, where it is mixed with the product gases.

In addition to the pellets that were used in the IH tests and described in the "Experimental Setup" section, pellets made with commercial ALSA (Aluminum S.A., Athens, Greece) alumina powder with larger particle size and higher impurities were also used for the solar tests. This material is used by ALSA for the electrolytic production of aluminum.

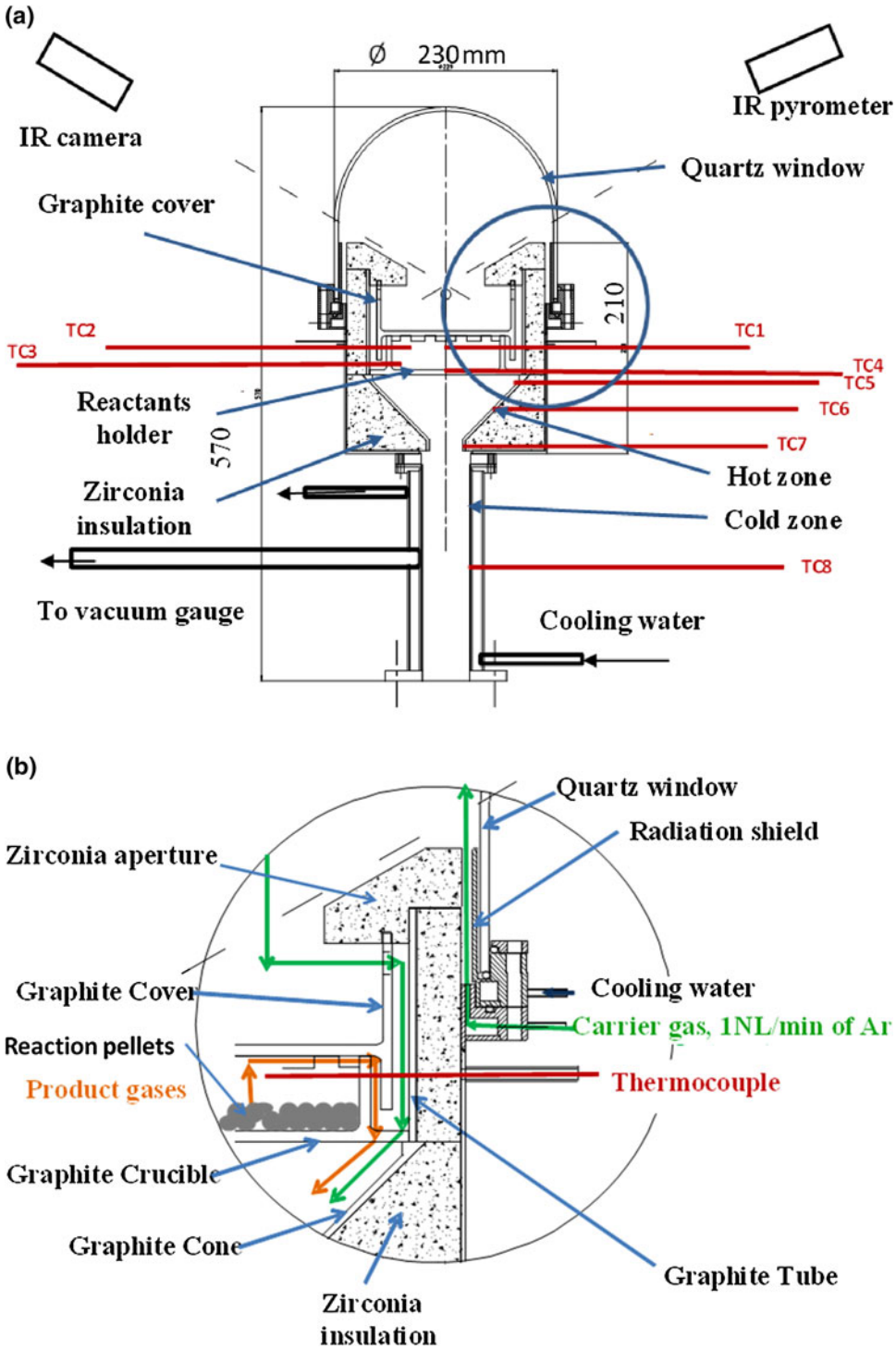

Fig. 5. Solar reactor design: (a) general view and (b) details.

Solar Reactor Experimental Setup

The principle scheme of the experimental setup is presented in Fig. 6. With a few exceptions, it is similar to the scheme of the IH reactor. The exit of the reactor is connected through trap, 5, to the dry vacuum system, 8 [model DRS1 made by Alcatel (Alcatel-Lucent, Paris, France), composed of an ACP40 multistage Roots pump (Alcatel-Lucent) operating without internal lubricant and a Roots blower RSV301B with bypass capable of 250 m^3/h peak pumping speed with 1000 mbar maximal continuous inlet pressure and 0.003 mbar ultimate pressure]. The DRS1 is equipped at its entrance with a filter, 6, and a liquid nitrogen trap, 7 (Nor-Cal Products, Yreka, CA, USA). Pressure

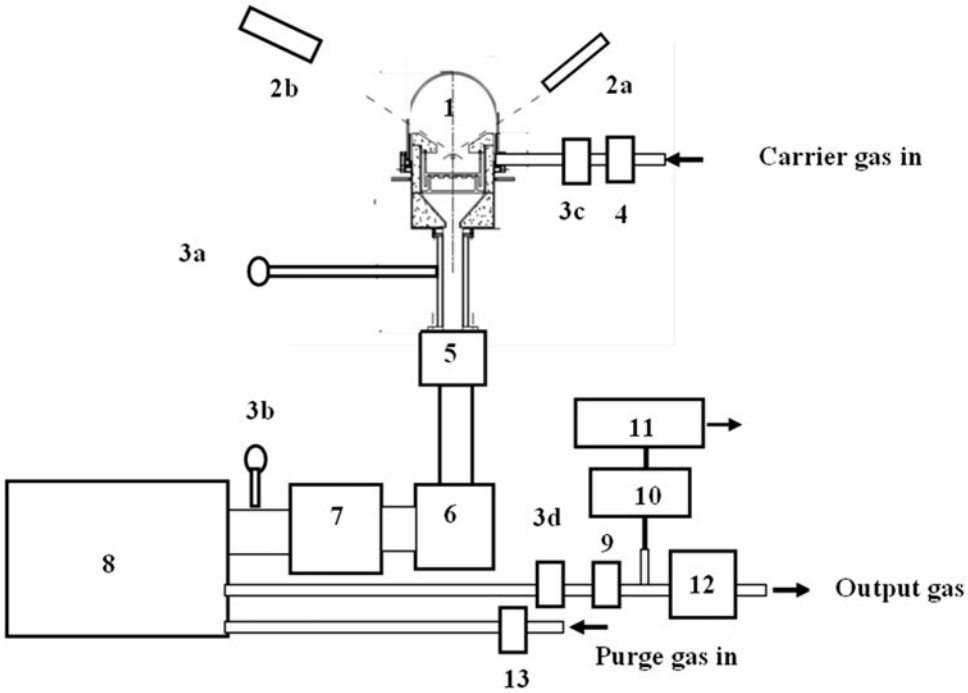

Fig. 6. A schematic layout of the experimental setup, 1-reactor, 2a-pyrometer, 2b-IR camera, 3a, b-vacuum gauges, 3c, d-pressure transmitters, 4, 13-inlet flow controllers, 5-trap, 6-filter, 7-liquid nitrogen trap, 8-dry vacuum system, 9-outlet flow meter, 10-diaphragm pump, 11-gas chromatograph, 12-IR analyzer (CO, CO_2, O_2).

is measured by two convection vacuum gauges (Model CVM-211; Instrutech Inc., Longmont, CO, USA); one of the gauges, 3a, is placed at the cooling tube of the reactor where the pressure is lower than the pressure in the hot reaction zone, and the second, 3b, is located at the entrance to the pumping system.

The flow rate of the carrier gas is monitored by a Tylan General flow controller, 4 (model FC260; Tylan General, Inc., San Diego, CA, USA), and the flow rate at the exit of the reactor is measured by a flow meter, 9 (model FM360), connected to the outlet of the DRS1. Input and output pressures are measured by pressure transmitters, 3c and 3d (STS Sensor, Danbury, CT, USA). The temperature of the quartz window is observed by an IR pyrometer, 2a (IMPAC model 3837230, 5.14 μm; LumaSense Technologies, Inc., Santa Clara, CA, USA), and its full image is obtained using an IR camera, 2b (FLIR model a320 with spectral range 7.5–13 μm; FLIR Systems, Inc., Boston, MA, USA).

The internal temperature of the solar reactor is measured by eight tungsten-rhenium (W–Re) thermocouples (type C) suitable for high temperatures (XMO-W5R26-U-125-30-H-HX-18; Omega, Stamford, CT, USA), which are placed in different areas of the hot and cold zones (Fig. 5a).

As mentioned above, product gases are mixed with the Ar carrier gas at the exit of the graphite crucible and evacuated through the filters and the nitrogen trap by the DVS. The exhaust gases are analyzed by a Siemens infrared analyzer Ultramat 23 (Siemens Aktiengesellschaft, Munich, Germany), 12, calibrated to detect CO, CO_2, and O_2. The absence of O_2 in the output gases before heating begins confirms that there are no leaks in the reactor. At the first stage of heating, the output gases also contain hydrogen and a small amount of CH_4 generated from hydrocarbon impurities in the charcoal. A small amount of the output gas is discharged by the diaphragm pump, 10, through a needle valve to the Varian 2900 gas chromatograph (Varian, Inc., Palo Alto, CA, USA), 11, for analysis.

All measured parameters are recorded on a personal computer every 5 s using Hydra Data Logger (Fluka Analytical, Buchs, Switzerland).

Experimental Results and Discussion

The Typical Measured Parameters and their Treatment

Typical solar test results are presented in Fig. 7a, including temperatures at the lower and upper area of reactant layers, direct normal irradiance (DNI), in and out gas flow rates, pressure in the cold zone of the reactor (G_{up}) and in the entrance to the vacuum system (G_{down}), window temperature as measured by the pyrometer, temperature along the inner surface of the graphite cone, temperature of the water cooled tube, inlet and outlet pressure, and percent composition of CO, CO_2 and H_2. As explained above, the CO yield exhibits two peaks

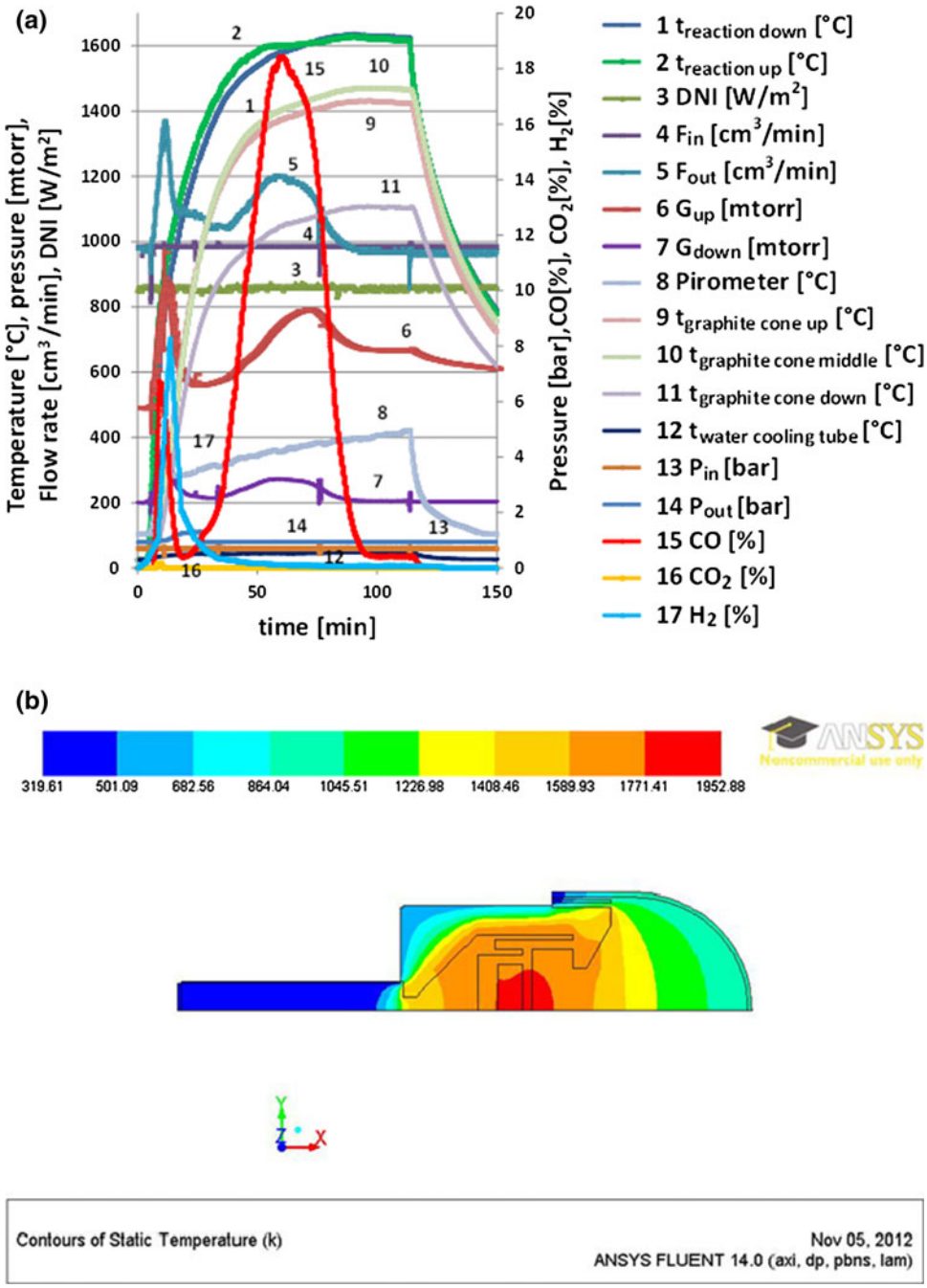

Fig. 7. (a) Typical solar test parameters and (b) calculated temperature distribution in K in the solar reactor (10.2 kW aperture input), FLUENT model.

(see the "Experimental Results" section). CO_2 is the main intermediate gas product in carboreduction; depending on the reaction temperature, it is fully or partially transformed to CO through the Boudouard reaction. Figure 7a shows the full transformation of CO_2 to CO. The maximum temperature in reaction zone was not higher than 1650°C, confirming the theoretical estimation using the FLUENT model and presented in Fig. 7b.

The quartz window is reliably protected from the settling of reaction products and, as a result of additional external air cooling, maintains a temperature (300–400°C measured by pyrometer and IR camera) significantly lower than both the allowable limit (~800°C) and the temperature estimated by FLUENT modeling as presented in Fig. 7b.

The weight percentage of aluminum, alumina, and by-products deposited at different locations after reaction was determinate by XRD quantitative analysis through profile-fitted peaks.

The formulas used for estimation of the test characteristics are presented below. The main

Table II. Results of solar tests

Test No.	Average/ maximum reaction temperature t (°C)	Average/maximum CO partial pressure in the cooling tube area P_{CO} (mbar)	Ratio of average temperature to average CO partial pressure (°C/mbar)	Oxygen yield (%)	Al yield (weight conversion) (%)
1	1525/1600	0.04/0.073	39776	93	90
2	1442/1576	0.073/0.22	19619	79	39
3	1486/1551	0.17/0.39	8937	78	44
4	1579/1651	0.31/0.60	5114	–	–
5	1548/1637	0.186/0.39	8319	76	34
6	1528/1633	0.064/0.18	23815	91	74

Table III. The results of the quantitative XRD analysis

			Weight of deposits and residue in the sample holder (g)			
			Content of deposits (wt.% by quantitative XRD)			
Test No.	Mass of reacted pellets (g)	Mass of Al in reacted pellets (g)	Hot zone	Cold zone	Filters	Residual unreacted and by-product in the sample holder
1	8.02	2.68	0.53 **70.3% Al** 12.3% Al_4C_3 17.3% C	1.75 **89% Al** 11%Al_2O_3	0.47 **91%Al** 5.4% Al_4C_3 3.6%C	0.63 66.4 Al_4C_3 33.6%C
2	20.54	6.86	2.02 **8.8%Al** 18.3% Al_2O_3 31.5% Al_4C_3 15.2%Al_4CO_4 26.2%C	3.84 **27.2%Al** 72.8% Al_2O_3	0.62 2.7%Al 81.4% Al_2O_3 15.8%C	3.73 14.1% Al_2O_3[a] 71.2% Al_4C_3 14.3% Al_4CO_4 0.35%C
3	23.69	7.25	2.11 **7.5%Al** 34.5% Al_4C_3 32.5%Al_4CO_4 32.%C	3.97 **56.6% Al** 43.1% Al_2O_3 0.3% Al_4C_3	0.71 **33.5%Al** 31.3% Al_2O_3 35.2%C	6.61 7.3% Al_2O_3[a] 69% Al_4C_3 20.2% Al_4CO_4 3.6%C
4	33.33	11.13	3.38 **28.1% Al** 4.1% Al_2O_3 18.7% Al_4C_3 38% Al_4CO_4 11% C	6.6 **42.3% Al** 33.5% Al_2O_3 25% Al_4C_3	1.41 **3.1% Al** 79.4% Al_2O_3 12.1% Al_4C_3	4.22 98.5% Al_4C_3 1.5% C
5	29.54	9.87	2.46 **22% Al** 40.2% Al_4C_3 19.3% Al_4CO_4 3.7% C	6 **54.6% Al** 21.6% Al_2O_3 17.3% Al_4C_3	2.57 98.3% Al_2O_3 1.76% Al_4C_3	2.62 94.6% Al_4C_3 5.5% C
6	20.35	6.80	1.87 **29% Al** 44.4% Al_4C_3 31.5% Al_4CO_4	5.33 **92.7% Al** 7.2% Al_2O_3 0.5% Al_4C_3	1.74 **50% Al** 7% Al_4C_3 40% Al_4C_3	0.79 86.3% Al_4C_3 13% C

[a]Alumina in unreacted pellets.

parameters including CO partial pressure, reaction temperature, and DNI were averaged by integrating over reaction time $f(\tau)$ as measured from the beginning (τ_1) to the end (τ_2) of the second CO peak, which contains oxygen atoms from reacted alumina:

$$f(\tau)_{\text{avg}} = \frac{\int_{\tau_1}^{\tau_2} f(\tau)d\tau}{\tau_2 - \tau_1} \quad (3)$$

The oxygen balance of the reaction was calculated as the number of moles of CO in its second

peak divided by the number of oxygen atoms in the reacted alumina:

$$\text{Oxygen yield} = \frac{\text{number of moles CO}}{3 \times \text{ number of moles reacted } Al_2O_3} \quad (4)$$

The aluminum yield was estimated as the total weight of pure aluminum in the deposits divided by the weight of aluminum in the reacted pellets.

$$\text{Aluminum yield} = \frac{\text{weight of pure Al in deposits}}{\text{weight of pure Al in reacted } Al_2O_3} \quad (5)$$

Solar Tests Results

The results of tests at various CO partial pressures and different weather and temperature conditions are presented in Table II (temperature values depend on DNI and presence of clouds). It can be seen that the conversion decreases and difference between oxygen and aluminum yield increases with decreasing temperature and increasing CO partial pressure.

Table III presents results of quantitative XRD analysis from Profile-Fitted Peaks for samples from different sites in the reactor (amount of pure aluminum was marked with bold). Samples with a significant amount of pure aluminum were deposited at the exit of the graphite cone on a sublayer of carbide, on the internal surface of the water cooled tube, and in the filters. Aluminum carbide and oxycarbide were formed both on hot sites as a result of carbonization of deposited Al when temperatures were not high enough to prevent the deposition, and in the sample holder as by-products of the forward reaction during the initial preheating and when reaction temperature was not high enough. The presence of corundum in the cold zone is explained by volatile suboxide that arrives there generally during the preheating phase. During its condensation, the suboxide can be transformed to alumina and aluminum according to Eq. 1. In tests with significant amount of reactants, the presence of carbide in the cold zone and the filters can be explained by the sweeping of residual carbide powder from the reactant holder.

Aluminum Morphology

Examples of aluminum deposits from various locations are presented in Fig. 8. These images show Al films and powders (50–90% Al, depending on reaction temperature and CO partial pressure) settled on the water-cooled surface of the exit tube at a temperature of ~50°C (Fig. 8a), and solidified condensate aluminum deposited on top of insulating layers of aluminum carbide and oxycarbide that were first formed at a temperature of ~1100°C on the surfaces at the exit of the graphite cone (Fig. 8b, c).

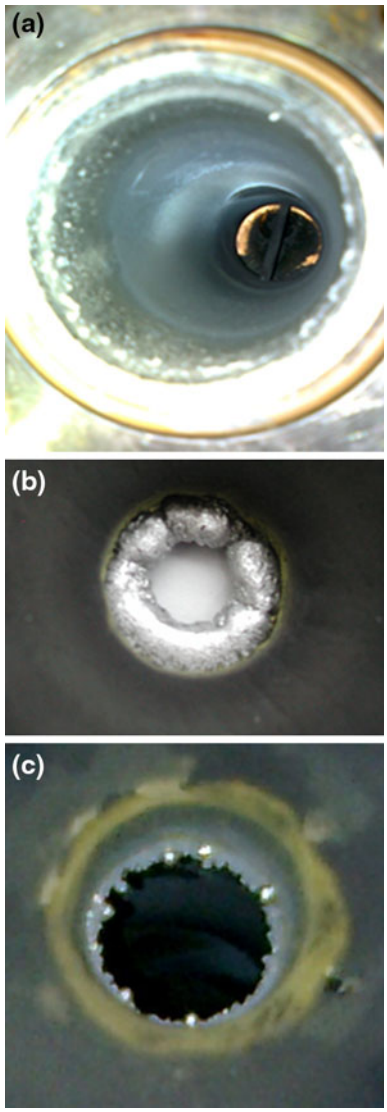

Fig. 8. Examples of deposited aluminum: (a) Al film and powder on water-cooled tube; (b, c) solidified condensate liquid aluminum on insulating layer of aluminum carbide and oxycarbide at the exit of graphite cone for tests with larger (b) and smaller (c) amounts of reactant pellets.

Typical SEM images and XRD spectra of aluminum from cold deposit sites are presented in Fig. 9.

The morphology of aluminum deposited on the water-cooled pipe in the cold zone differs significantly from the spherical drops deposited on hot sites, resembling submicron and nanocrystalline structure.[11] Another sample from the cold zone exhibits higher amorphous content with small aluminum peaks. It is assumed that this sample together with nanocrystalline aluminum constitutes an amorphous phase that can be associated with the alumina formed during deposition of volatile aluminum suboxide on the cold site according to Eq. 1.

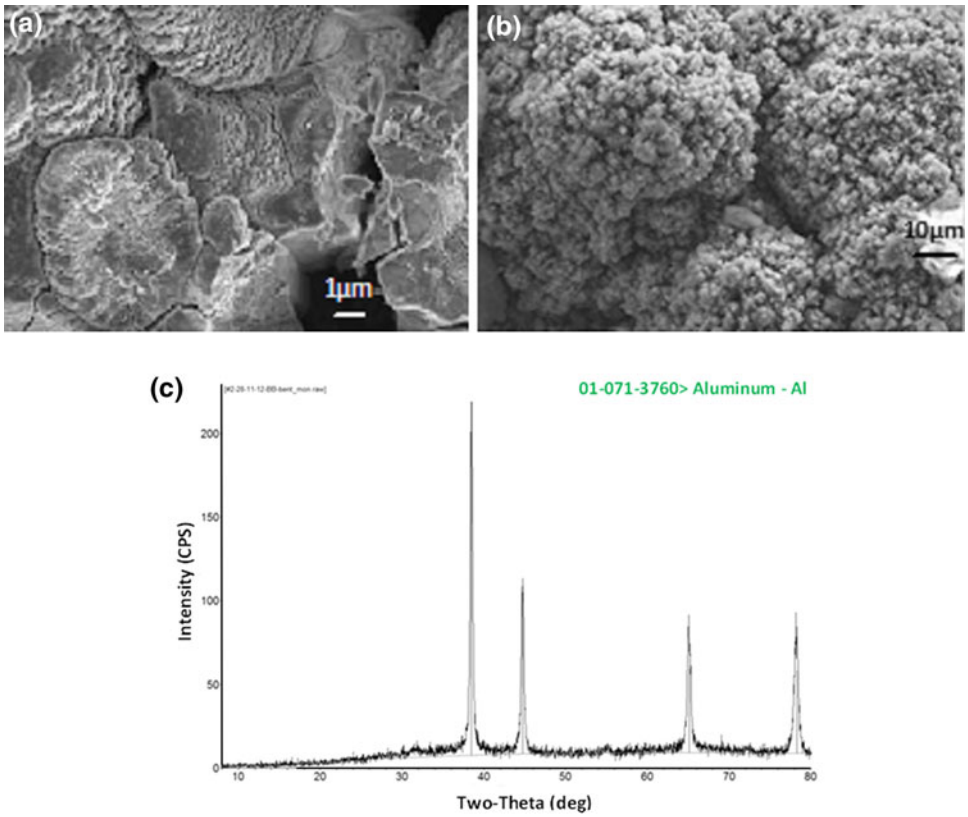

Fig. 9. Typical SEM images of aluminum deposited on the cold zone referring to tests with different amounts of the reacting pellets magnified by: (a) 10 K, (test No. 1); (b) 2 K, (test No. 6), and (c) their typical XRD spectrum.

SUMMARY AND CONCLUSIONS

The actual pumping power consumption by the Roots DVS was estimated, and it was shown that for CO partial pressure lower than 0.2–0.3 mbar, the pumping energy can exceed the energy consumption in the industrial Hall–Heroult electrolytic process. Thus, the reaction conditions are optimized by a balance between decreasing the reaction temperature, which requires lower product gas partial pressure, and increasing pumping volumes, which demands higher pumping power.

Primary tests in IH furnace were performed using pellets made of 10-μm alumina powder, charcoal, and sugar powder as a binder. It was shown that the forward reaction can be fully completed when the minimal temperature in the reaction zone was above 1500°C and the time-averaged CO partial pressure was below 0.2 mbar. Increasing the average CO partial pressure to 2.6 mbar compels a 150–200°C increase in the corresponding reaction temperature.

Theoretical calculations of the effective emissivity and the temperature distribution along parts of the tubular IH reactor were performed to correlate the real temperatures in the reaction zone and at the deposit sites with the remote measurement temperatures and to correlate the maximal content of aluminum with the temperatures at these sites. It was also shown that to avoid oxidation and carbonization of the deposited aluminum when the CO partial pressure is in the range of tenths of millibars, the temperature at the deposit site should be below 600–700°C.

A solar reactor was designed and built based on the numerical modeling realizing a sharp temperature decrease in the transition space between the hot and the cold zones.

One of the solar concentrating facilities at the Weizmann Solar Tower with 10-kW capacity and solar concentration of 5000 suns was used for the solar testing.

Solar tests were carried out at different CO partial pressures and reaction temperatures. It was confirmed that the conversion achieved depends strongly on the reaction temperature and CO partial pressure; higher temperature and lower CO partial pressure result in higher aluminum yield. The best results (~90% aluminum conversion) were obtained in tests with an average reaction temperature of 1525°C and a CO partial pressure of 0.04–0.06 mbar near the cold zone.

A major drawback of the current solar reactor is the relatively slow initial heating rate, which required about 40 min to reach the appropriate reaction temperature. During this startup time, the low temperature favors formation of undesirable volatile and solid by-products in the forward and backward reactions. To save pumping power and avoid these

by-product formation in future tests, it is advisable to preheat the reactor to operation temperature before introducing reactants, and then to feed the reactants continuously at a controlled rate as a function of the DNI and the temperature in reaction zone.

The morphology of the produced pure aluminum depends on the temperature at the deposit site. In the cold zone (~50°C), fast cooling forms nanometers and submicron aluminum particles, whereas it is possible to obtain liquid aluminum at deposit sites where the temperature close to the aluminum melting point exists.

ACKNOWLEDGEMENTS

The authors would like to express their gratitude to Mr. Adi Arnon for his assistance in preparing and carrying out the experiments, to Dr. Yishai Feldman, and to Dr. Konstantin Gartsman for performing the XRD and SEM analyses of the powders before and after the tests. The research leading to these results was supported by the European Union Seventh Framework Programme (FP7/2007-2013) under Grant agreement NER/FP7EN/249710/ENEXAL.

REFERENCES

1. I. Vishnevetsky, R. Ben-Zvi, and M. Epstein (Paper presented at SolarPACES—*Proc. of 18th International Conference on Concentrating Solar Power and Chemical Energy System*, Marrakesh, Morocco, 2012).
2. M. Halman, A. Frei, and A. Steinfeld, *Energy* 32, 2420 (2007).
3. M. Halman, A. Frei, and A. Steinfeld, *Miner. Process. Extr. Metall. Rev.* 32, 247 (2011).
4. M. Kruesi, M.E. Galvez, M. Halmann, and A. Steinfeld, *Metall. Mater. Trans. B* 42, 254 (2011).
5. W.J. Kroll and A.W. Schlechton, *J. Electrochem. Soc.* 93, 247 (1948).
6. I. Vishnevetsky and M. Epstein (Paper presented at SolarPACES—*Proc. of the 17th International Conference on Concentrating Solar Power and Chemical Energy System*, Granada, Spain, 2011).
7. A. Roine, *HSC Chemistry Computer Code, V. 5.0* (Pori, Finland: Outokumpu Technology, 2006).
8. ANSYS Fluent Version, axi, double precision, pressure-based, laminar, Revision: 14.0.0 for the ANSYS Release Version 14.0, Build Time: Oct 25 13:06:24 Build Id: 10398 (ANSYS, Inc., 2011).
9. Elmerfem-trunk.tar-dated 05/07/11; http://www.csc.fi/elmer.
10. M.F. Modest, *Radiative Heat Transfer* (New York: McGraw-Hill, 1993).
11. O.N. Senkov, S.V. Senkova, J.M. Scott, and D.B. Miracle, *Mater. Sci. Eng. A* 393, 2005 (12).